(Received 19 September 2025, Accepted 3 November 2025, Scheduled 7 December 2025)

Slot-Enhanced Next-Generation Wireless Antenna for Millimeter-Wave Applications for SDG-9 and SDG-11

Swati V. Yadav[1,*], Manish V. Yadav[2], Saraswati Kulkarni[3], Vikas Gupta[4], and Tanweer Ali[5]

[1]*Department of Instrumentation and Control Engineering, Manipal Institute of Technology Manipal Academy of Higher Education, Manipal, Karnataka 576104, India*
[2]*Department of Aeronautical and Automobile Engineering, Manipal Institute of Technology Manipal Academy of Higher Education, Manipal, Karnataka 576104, India*
[3]*Department of Biomedical Engineering, Manipal Institute of Technology Manipal Academy of Higher Education, Manipal, Karnataka 576104, India*
[4]*Department of Electronics and Telecommunication Engineering Vidyavardhini's College of Engineering and Technology, Maharashtra, India*
[5]*Department of Electronics and Communication Engineering, Manipal Institute of Technology Manipal Academy of Higher Education, Manipal 576104, India*

ABSTRACT: This article presents a slot-enhanced compact antenna tailored for next-generation millimeter-wave communication systems. The design, implemented on an FR4 substrate with dimensions of $15 \times 16 \times 1.5\,\text{mm}^3$, was optimized using CST Microwave Studio and validated through fabrication and experimental testing. At 9.1 GHz, the antenna exhibits an electrical size of $0.45\lambda \times 0.48\lambda \times 0.045\lambda$, confirming its suitability for integration into modern high-frequency platforms. The measured and simulated results demonstrate an ultra-wide impedance bandwidth of approximately 166%, covering 9.1–100 GHz with a primary resonance observed at 45.45 GHz. Throughout this wide operating spectrum, the antenna maintains stable radiation characteristics, achieving a peak gain of 8.91 dBi and efficiency close to 90%. The slot-based geometry enables excitation of multiple resonant modes, ensuring wideband operation while maintaining compactness. With its robust performance across multiple frequency bands, the proposed antenna is a strong candidate for applications in X-band radar, Ku- and Ka-band satellite communications, K-band sensing, V-band short-range links, W-band automotive radar, and future 6G wireless networks.

1. INTRODUCTION

The exponential growth of wireless communication systems has created an increasing demand for antennas that can deliver high performance across wide frequency ranges while maintaining compact dimensions. With the emergence of advanced technologies such as 5G, 6G, satellite communication, radar, and security imaging systems, antennas are expected to support multi-band operation, high gain, stable radiation, and efficiency within compact footprints. Among various antenna types, microstrip patch antenna (MPA) has attracted significant attention due to its low profile, lightweight structure, ease of fabrication, and suitability for integration with modern communication circuits. However, conventional patch antennas are limited by narrow bandwidth, relatively low gain, and sensitivity to substrate losses, which restrict their application in next-generation high-frequency systems.

To overcome these challenges, researchers have explored several approaches, including the use of slots, parasitic patches, defected ground structures (DGSs), and novel feed techniques to enhance bandwidth and improve radiation performance. For instance, introducing U-slots, circular cut-outs, and etching patterns into the patch or ground plane has proven effective in exciting multiple resonant modes and achieving wideband characteristics [20, 21]. Similarly, parasitic patch configurations have been employed to increase coupling and extend impedance bandwidth [22]. For instance, introducing U-slots, circular cut-outs, and etching patterns into the patch or ground plane has proven effective in exciting multiple resonant modes and achieving wideband characteristics. Similarly, modifications in feedline geometry and substrate materials have also contributed to improved impedance matching and higher efficiency. These strategies have made MPAs highly adaptable to applications spanning X-, Ku-, K-, Ka-, V-, and W-bands, which are critical for both present and future communication systems.

The upcoming 6G communication networks will operate predominantly in millimeter-wave and terahertz bands, demanding antennas capable of delivering ultra-wide bandwidth, high data rates, and low latency. Unlike traditional cellular communication, 6G will require antennas to operate efficiently under challenging propagation conditions while supporting diverse use cases such as Internet of Things (IoT), autonomous vehicles, immersive virtual reality, and advanced imaging technologies. In this context, compact and high-performance antennas are key enablers for ensuring system reliability and scalability. In addition to communication, wideband antennas are increasingly important in radar and sensing applications, where high resolution and accurate target detection depend on stable radiation

* Corresponding author: Swati Varun Yadav (yadav.swati@manipal.edu).

and wide frequency coverage. Automotive radar in the W-band and satellite communication in the Ka- and Ku-bands are prime examples of real-world systems where antenna compactness, gain, and efficiency are equally important.

Microstrip patch antennas (MPAs) have long been valued for their simple geometry, low profile, and compatibility with modern communication platforms. Numerous modifications have been introduced to improve performance, particularly in terms of bandwidth, gain, and efficiency. Mishra et al. [1] provided a detailed review of geometry-based and ground-plane modifications, identifying techniques such as slotting, defected ground structures, and parasitic loading as effective means for bandwidth enhancement. These foundational methods have been widely adopted in subsequent designs.

With the advent of 5G, attention shifted toward compact antennas operating in the millimeter-wave range. Przesmycki et al. [2] reported a broadband 28 GHz design using a Rogers substrate, achieving 5.57 GHz bandwidth and approximately 80% efficiency. Similarly, Imran et al. [3] designed a compact patch operating at 38 and 54 GHz, where a 1×4 array configuration provided up to 12 dB gain, demonstrating the necessity of arrays to overcome path loss at higher frequencies. Verma et al. [8] proposed a small 10.15 GHz patch on FR-4, highlighting miniaturization but also pointing out efficiency challenges inherent in low-cost substrates.

Various geometry-based approaches have been explored to address these challenges. Khidre et al. [4] introduced a U-slot configuration capable of achieving dual-beam radiation, while Baudha et al. [5] investigated U-shaped patches with partial ground planes for mobile satellite services. Ghosh et al. [7] showed that defected patch surfaces improved polarization purity, reducing cross-polarization. These studies highlight that geometry modifications are powerful but often come with trade-offs in terms of complexity and design sensitivity. Practical fabrication aspects have also been emphasized. Kurniawan and Mukhlishin [6] argued that validating simulation with fabricated prototypes is essential, as small deviations significantly affect high-frequency behavior. Looking beyond 5G, attention is moving into the terahertz (THz) domain for 6G. Akyildiz et al. [9, 10] and Han and Chen [11] discussed fundamental propagation challenges, such as severe attenuation and molecular absorption, that demand new modeling and antenna solutions. Rappaport et al. [12] and Jornet et al. [13] further outlined system-level opportunities above 100 GHz, noting potential applications in high-speed data, sensing, and security. Singh et al. [14] surveyed antenna developments at 30, 60, and 120 GHz, underlining substrate choice and efficiency as key design bottlenecks. Recent works address these challenges with innovative designs. Min et al. [15] presented a radome-optimized series-fed W-band array with high gain and efficiency for automotive radar, while Al-Hiti et al. [16] demonstrated broadband and multiband mmWave patches with efficiencies approaching 94%. At 100 GHz, Perez-Palomino et al. [17] showcased electronically controlled reflect arrays, offering high gain and beam agility. At lower mmWave frequencies, compact designs continue to attract interest: Kumar et al. [18] reported an ultra-compact 28 GHz arc-shaped patch, and Muttair et al. [19] introduced a multi-band MIMO antenna spanning 17–100 GHz, a significant step toward versatile 6G hardware.

In summary, the literature demonstrates steady progress from bandwidth enhancement methods [1, 4, 7] to compact and broadband mmWave designs [2, 3, 8], and further to multiband and W-band solutions [15, 16, 19]. While system-level studies [9, 14, 17] establish the direction toward mmWave and 6G, the practical design trade-off among compactness, bandwidth, and fabrication feasibility remains an open challenge. This motivates the development of new antennas that can provide wideband operation, high efficiency, and compact form factors suitable for the integration into future 6G platforms.

In the following sections, this study highlights the novel design and realization of a compact slot-enhanced ultra-wideband antenna that achieves outstanding performance across the 9.1–100 GHz frequency spectrum using a cost-effective FR4 substrate. The novelty of this work lies in the unique hybrid configuration of circular and rectangular slots, whose optimized coupling and spacing enable the excitation of multiple resonant modes and the achievement of an exceptionally wide impedance bandwidth of approximately 166%, along with a peak gain of 8.91 dBi and an efficiency close to 90%. Unlike conventional slotted or DGS-based antennas, the presented structure undergoes a systematic four-stage design evolution, where each geometrical refinement contributes to enhanced impedance matching, radiation stability, and broadband response. The excellent correlation between simulated and experimental results confirms that the wideband characteristics originate from the antenna's genuine electromagnetic behavior rather than simulation artifacts.

2. GRAPHICAL ABSTRACT

Figure 1 shows the graphical abstract that illustrates the complete design, fabrication, and evaluation process of the proposed compact multi-band antenna intended for millimeter-wave and 6G applications.

The workflow begins with (a) Simulation using Computer Simulation Technology (CST), where the antenna geometry is modelled and optimized through full-wave electromagnetic simulations. These simulations allow the precise tuning of design parameters to achieve wideband impedance performance and stable radiation characteristics. Following the design stage, (b) Antenna Fabrication is carried out on an FR4 substrate using standard photolithographic techniques. The fabricated prototype closely replicates the simulated structure, ensuring that the experimental model aligns with the proposed design.

The next stage, (c) Antenna Testing and Measurement involve characterizing the antenna using a Vector Network Analyzer (VNA). The prototype is placed inside an anechoic chamber to minimize reflections and ensure accurate measurement of reflection coefficients (S_{11}). The measured results are then compared with simulated data, confirming the consistency of the design across the targeted frequency spectrum.

Finally, (d) Results and Discussion present a detailed analysis of the antenna's performance. The results include simulated and measured S_{11} curves, which validate the ultra-wideband re-

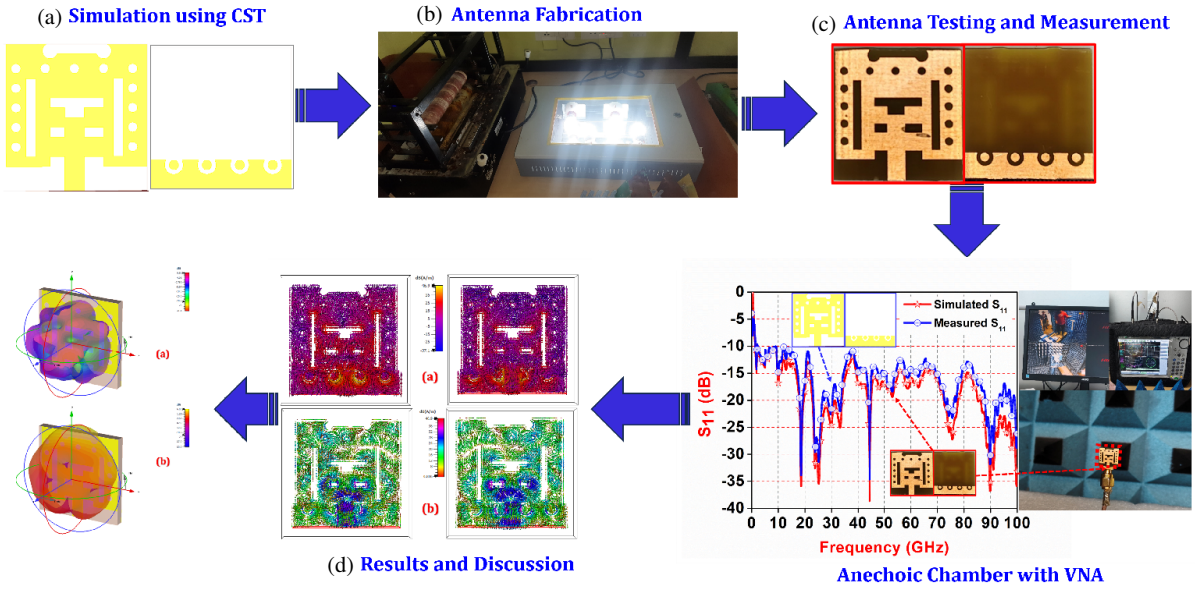

FIGURE 1. Graphical abstract, (a) simulation in CST, (b) fabrication, (c) testing and measurement, and (d) comparison of simulated and measured results.

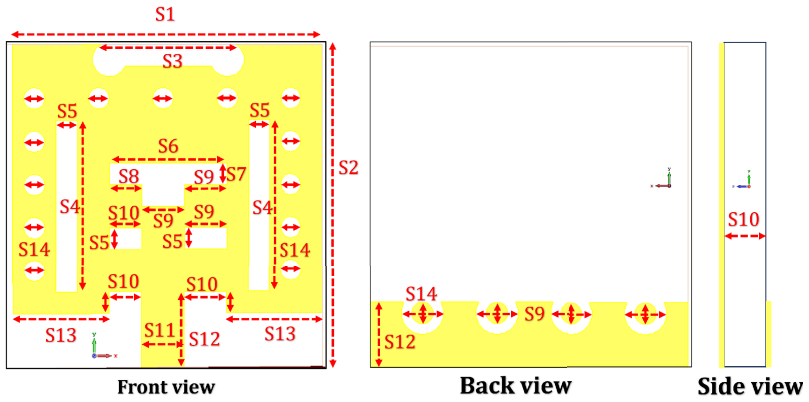

FIGURE 2. Conceptual design of an antenna.

sponse from 9.1 GHz to 100 GHz. Radiation patterns at different frequencies demonstrate stable omnidirectional behavior, while surface current distributions highlight the effective excitation of multiple resonant modes. The antenna achieves a high peak gain and efficiency, confirming its suitability for modern high-frequency systems. Overall, the graphical abstract conveys the systematic workflow from design to experimental verification. It highlights how the compact antenna, through simulations, fabrication, and rigorous measurements, demonstrates outstanding broadband performance.

3. ANTENNA STRUCTURE AND EVOLUTION

Figure 2 shows that the proposed planar antenna structure is illustrated through its front, back, and side views. The design is implemented on an FR4 substrate and incorporates multiple slots, circular cut-outs, and feedline modifications to enhance its broadband performance. The front view highlights the central radiating patch with surrounding circular slots and etched sections that help in exciting multiple resonant modes. The back view features symmetrical circular cut-outs that improve impedance matching and overall radiation efficiency, while the side view represents the substrate thickness, which influences the gain and bandwidth.

Table 1 shows that the proposed antenna design is governed by fourteen geometric parameters (S_1–S_{14}), each optimized to achieve broadband operation and stable radiation across the 9.1–100 GHz range. The overall size of the structure is defined by $S_1 = 15$ mm and $S_2 = 16$ mm, which set the physical boundaries and electrical dimensions of the substrate. The top slot ($S_3 = 6.2$ mm) and vertical slots on either side

TABLE 1. Parameters and values of the proposed antenna.

Parameters	S_1	S_2	S_3	S_4	S_5	S_6	S_7
Values	15	16	6.2	8	1	5.5	1
Parameters	S_8	S_9	S_{10}	S_{11}	S_{12}	S_{13}	S_{14}
Values	1.5	2	1.5	2	3.5	5.5	0.5

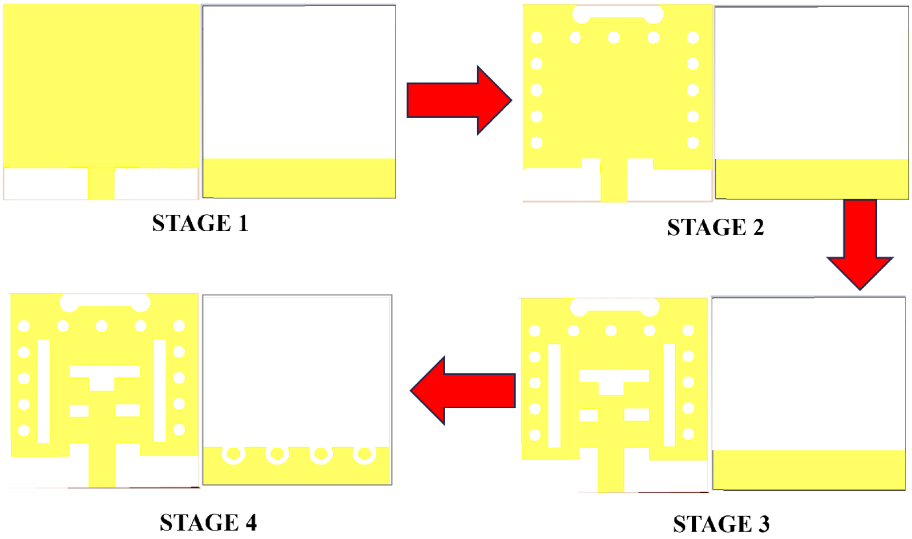

FIGURE 3. Antenna evolution from Stage 1–4.

($S_4 = 8$ mm) introduce additional resonant paths that enhance the impedance bandwidth. Narrow slots such as $S_5 = 1$ mm and $S_7 = 1$ mm are responsible for controlling current flow and tuning higher-order resonances, while the central slot length ($S_6 = 5.5$ mm) strengthens mode excitation and coupling. The inclusion of a horizontal slot ($S_8 = 1.5$ mm) and circular cut-outs ($S_9 = 2$ mm) improves impedance matching and contributes to multi-resonant behavior. Feed-related dimensions, including $S_{10} = 1.5$ mm and feedline width $S_{11} = 2$ mm, are adjusted to ensure proper matching with the standard 50 Ω input. The lower cut-out length ($S_{12} = 3.5$ mm) and ground slot ($S_{13} = 5.5$ mm) expand the operational bandwidth by reducing mismatches and improving return loss. Finally, the spacing between the circular slots ($S_{14} = 0.5$ mm) maintains symmetry in current distribution, which stabilizes the radiation performance. Through the collective influence of these parameters spanning patch slots, cut-outs, and feed adjustments the antenna achieves wide impedance coverage, high efficiency, and reliable radiation characteristics suitable for modern millimeter-wave communication systems.

4. EVOLUTION OF THE PROPOSED ANTENNA

Figure 3 shows that the evolution of the proposed antenna is illustrated through four systematic stages, where each modification is introduced to enhance bandwidth, resonance characteristics, and overall radiation performance.

Stage 1: The design begins with a basic rectangular radiating patch connected to a microstrip feedline and supported by a partial ground plane. This initial structure generates a limited number of resonant frequencies, with poor impedance bandwidth, making it unsuitable for ultra-wideband millimeter-wave applications. Nonetheless, it serves as the foundation for further modifications.

Stage 2: In the second stage, symmetrical circular slots are etched along both vertical edges of the radiating patch, with a curved slot at the top. These modifications help in exciting additional resonant modes by altering the surface current distribution. As a result, the antenna begins to exhibit improved impedance matching and wider bandwidth than Stage 1, although the performance still requires enhancement for higher-frequency operations.

Stage 3: The third stage introduces rectangular slots within the central patch region. These inner slots contribute to better coupling and effective excitation of multiple higher-order modes. The modification significantly improves return loss characteristics and strengthens resonance stability across the desired frequency range. However, additional fine-tuning is necessary to achieve ultra-wideband behavior.

Stage 4: In the final stage, circular cut-outs are etched at the bottom edge of the radiating structure, while retaining the previously introduced slots. This modification optimizes impedance matching and expands the operational bandwidth, allowing the antenna to achieve ultra-wideband performance from X-band through W-band. The final geometry also provides stable radiation patterns, high gain, and good efficiency, making it highly suitable for 5G, 6G, radar, and satellite applications.

Figure 4 shows the return loss (S_{11}) characteristics for the antenna design across its four evolutionary stages, highlight-

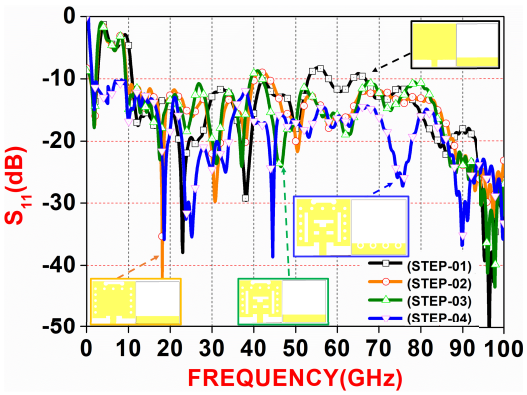

FIGURE 4. All stages S_{11} parameter from Stage 1–4.

ing how each structural modification contributes to impedance bandwidth enhancement and resonance stability.

Stage 1: The initial configuration (black curve) shows limited performance with only a few resonant dips, primarily confined to the lower frequency region below 20 GHz. The impedance matching is not consistent, and wideband behavior is absent, demonstrating that the simple patch with a partial ground is insufficient for millimeter-wave applications.

Stage 2: With the introduction of side slots, the antenna response improves (orange curve). Multiple resonant modes are excited, extending the operational range up to nearly 40 GHz. However, the return loss still fluctuates and fails to achieve stable wideband characteristics across the entire spectrum.

Stage 3: Further structural modifications, including additional slots and etchings, result in the green curve response. This stage shows significant improvement, with several well-defined resonant dips spanning a broader range of frequencies. The impedance bandwidth is extended, and resonance stability becomes more noticeable, especially in the mid-frequency range around 40–70 GHz.

Stage 4: The final optimized structure (blue curve) exhibits the best performance, achieving ultra-wideband operation from below 10 GHz up to nearly 100 GHz. The return loss remains consistently below -10 dB across most of the spectrum, with multiple strong dips at key frequency bands. This stage confirms the successful design evolution, as the antenna now provides excellent impedance matching, stable resonances, and wideband behavior.

Figure 5 presents the parametric analysis of the proposed antenna with respect to the circular slot diameter denoted as S_5. Three variations of S_5 were examined: 0.5 mm, 1 mm, and 1.5 mm, to observe their impact on the return loss (S_{11}) response across the 0–100 GHz frequency spectrum. When $S_5 = 0.5$ mm (black curve), the antenna exhibits multiple resonant dips but with weaker impedance matching at higher frequencies. Increasing the slot size to $S_5 = 1$ mm (red curve) significantly improves bandwidth and resonance stability, resulting in better matching across several bands. Further enlarging the slot to $S_5 = 1.5$ mm (blue curve) introduces deeper resonances at certain frequencies but causes slight shifts in resonant positions. Overall, the optimized value of $S_5 = 1$ mm demonstrates the best balance, offering wide impedance bandwidth and stable resonances, making it the most suitable configuration for ultra-wideband operation.

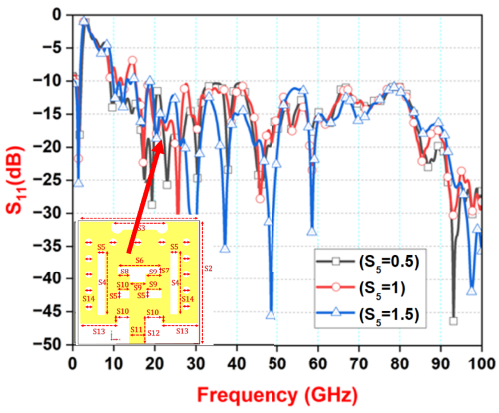

FIGURE 5. Simulated parameter sweep 'S_5'.

Figure 6 shows the effect of varying the parameter S_{14}, which represents the spacing between the circular slots placed along the sides of the radiating patch. Three different values of S_{14} were analyzed: 0.4 mm, 0.5 mm, and 0.6 mm, to evaluate their influence on the return loss (S_{11}) response.

When $S_{14} = 0.4$ mm (black curve), the antenna achieves multiple resonant dips; however, some mismatches appear at higher frequencies. Increasing the spacing to $S_{14} = 0.5$ mm (red curve) improves impedance matching and provides more uniform resonance behavior across the frequency spectrum. Further enlarging the spacing to $S_{14} = 0.6$ mm (blue curve) slightly shifts the resonances, producing deeper dips around certain bands but with minor variations in bandwidth. Overall, the optimized value of $S_{14} = 0.5$ mm offers the best trade-off, delivering consistent wideband performance and stable impedance matching up to 100 GHz.

Figure 7 shows that the return loss characteristics of the proposed antenna were obtained through both simulation and experimental validation. The antenna was first designed and optimized using CST Microwave Studio, where full-wave electromagnetic simulations were carried out to achieve wideband impedance matching. The simulated S_{11} response, shown in red, demonstrates multiple resonant dips extending from below 10 GHz to nearly 100 GHz, confirming the antenna's ultra-wideband behavior.

To validate the design, the antenna was fabricated on an FR4 substrate in the antenna laboratory, following the optimized geometrical parameters. For experimental characterization, the prototype was tested inside an anechoic chamber to ensure a controlled, reflection-free environment. A Vector Network Analyzer (VNA) was used to measure the reflection coefficient, with the measured S_{11} plotted in blue. The comparison between simulated and measured results shows a strong agreement, with both responses exhibiting multiple resonant frequencies and wide impedance bandwidth. Minor deviations between the two curves can be attributed to fabrication tolerances, material imperfections, and connector losses. Despite these variations, the measured S_{11} remains consistently below -10 dB across most of the operating spectrum, validating the reliability of the simulated model.

It should be emphasized that while FR4 inherently suffers from higher dielectric losses above 1015 GHz, its use in this work was intended to provide a cost-effective and practical demonstration of the antenna's design feasibility rather than to claim superior material performance. The observed wide impedance bandwidth (9.1100 GHz) is primarily the outcome of the optimized slot geometry and coupling arrangement, which enable the excitation of multiple resonant modes. Experimental verification using a Vector Network Analyzer (VNA) and measurements conducted in an anechoic environment validate the broadband response, with the antenna maintaining an efficiency of nearly 90% within the 1060 GHz region, where FR4's dielectric losses remain within acceptable limits. These findings confirm that the wideband characteristics

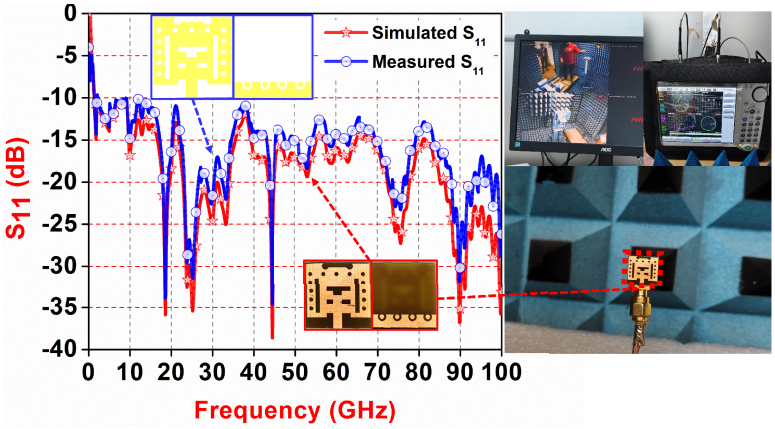

FIGURE 6. Comparison between simulated and measured S_{11} (reflection coefficient).

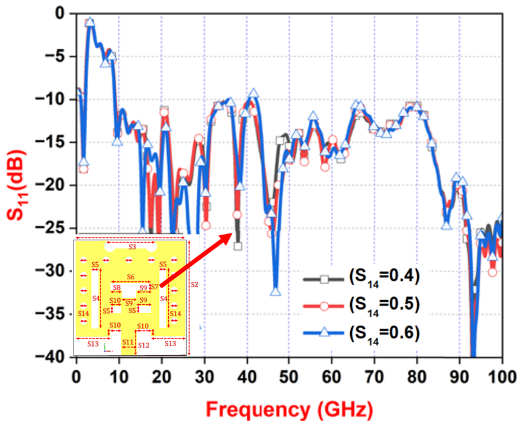

FIGURE 7. Simulated parameter sweep 'S_{14}'.

originate mainly from the electromagnetic design optimization rather than the intrinsic properties of the substrate.

The equivalent circuit of the planar antenna can be understood through the assignment of approximate R, L, and C values that capture its resonant characteristics. Operating at the 9.1 GHz band, the wavelength is around 33 mm, and the antenna's main radiating patch can be modeled as a parallel RLC network. Here, the resistance about 50 Ω represents radiation resistance.

5. EQUIVALENT CIRCUIT FOR ANTENNA (9.1 GHz)

5.1. Step 1. Wavelength and Frequency Relation

$$\lambda = \frac{c}{f} = \frac{3 \times 10^8}{9.1 \times 10^9} = 0.033\,\text{m}\,(33\,\text{mm})$$

5.2. Step 2. Main Patch RLC Resonator

- Resonant frequency $f_o = 9.1$ GHz
- Capacitance from edge fringing fields: $C = 0.3$ pF
- Inductance: $L = 1/(2\pi f_o)^2$, $C = 1.02$ nH
- Radiation resistance (R): typically 40–70 Ω for microstrip patches, take $R = 50\,\Omega$.

5.3. Step 3. Slots/Stub LC Tanks

Each slot introduces additional resonance.

- Slot LC Tank 1: $L = 0.8$ nH, $C = 0.25$ nH, resonance near 10 GHz
- Slot LC Tank 1: $L = 0.5$ nH, $C = 0.15$ pF, resonance near 14 GHz

5.4. Step 4. Parasitic Elements

Parasitic slots create further notches/stopbands.

- **Equivalent values:** $L = 1.5$ nH, $C = 0.2$ pF, resonance near 19.5 GHz,

Final Equivalent Circuit Values (for 9.1 GHz design)

- **Main patch (parallel RLC):** $R = 50\,\Omega$, $L = 1.02$ nH, $C = 0.3$ pF
- **Slot LC Tank 1:** $L = 0.8$ nH, $C = 0.25$ pF
- **Slot LC Tank 2:** $L = 0.5$ nH, $C = 0.15$ pF
- **Parasitic LC:** $L = 1.5$ nH, $C = 0.2$ pF

The proposed antenna operating at 9.1 GHz can be represented using an equivalent circuit as shown in Figure 8, model to analyze its impedance and resonant behavior. The starting point is the main radiating patch, which is modeled as a parallel RLC resonator. The capacitance originates from the fringing fields at the patch edges, taken as approximately 0.3 pF. At the operating frequency of 9.1 GHz, the inductance is calculated using the formula:

$$L = 1/(2\pi f_o)^2 C$$

Substituting the values gives $L \approx 1.02$ nH, while the radiation resistance is assumed to be 50 Ω, which falls within the expected range (40–70 Ω) for microstrip patches.

To account for additional resonances, slots etched in the patch are modeled as series LC tanks. The first slot introduces a resonance near 10 GHz with $L \approx 0.8$ nH and $C \approx 0.25$ pF, while the second slot generates a resonance around 14 GHz, represented by $L \approx 0.5$ nH and $C \approx 0.15$ pF. These slots are

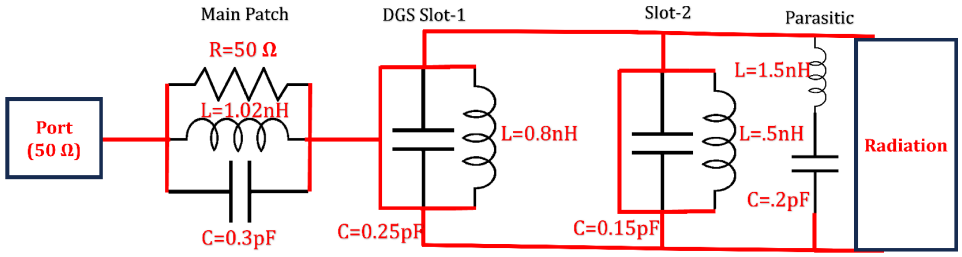

FIGURE 8. Equivalent circuit of the proposed antenna.

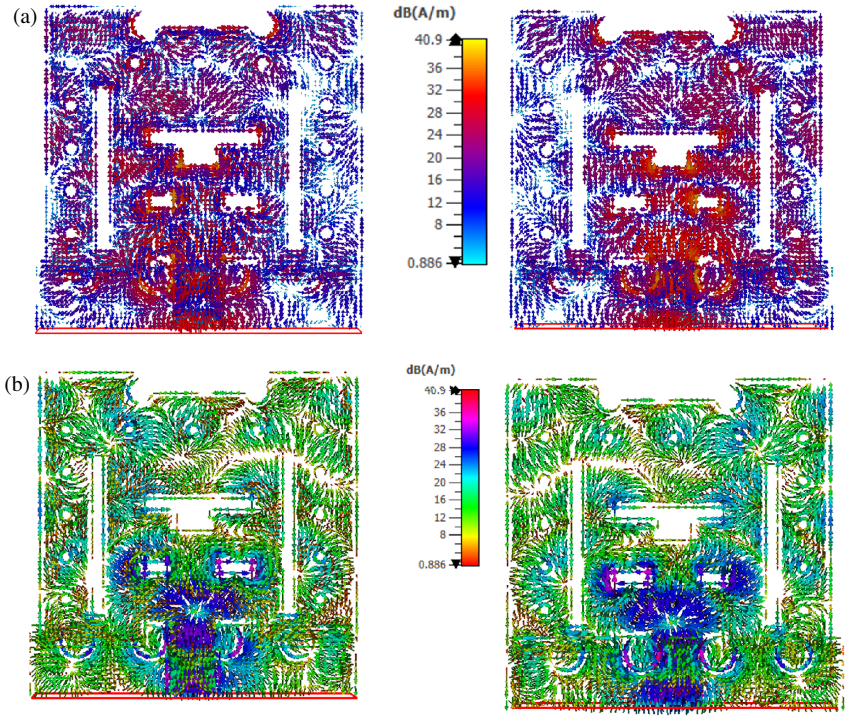

FIGURE 9. Surface current distribution of the antenna at (a) 20 GHz, (b) 45 GHz.

responsible for exciting multiple higher-order modes, which extend the impedance bandwidth.

Further refinements are introduced by parasitic elements, represented as another LC branch with $L \approx 1.5\,\text{nH}$ and $C \approx 0.2\,\text{pF}$, producing a resonance near 19.5 GHz. This improves impedance matching and helps suppress unwanted responses, contributing to the antenna's ultra-wideband behavior. Thus, the final equivalent circuit consists of the main patch RLC in parallel, accompanied by series LC tanks and parasitic branches. This combination effectively models the antenna's wideband impedance characteristics, explaining its ability to operate from 9.1 GHz up to 100 GHz with multiple resonant dips, stable matching, and enhanced bandwidth. These elements collectively form a multi-resonant equivalent circuit that accurately models the antenna's broadband impedance characteristics. The electrical circuit parameters for the proposed design are presented in Table 2.

The developed equivalent RLC network provides a simplified analytical representation of the antenna's resonant characteristics around 9.1 GHz. In this model, the main radiating patch is represented by a parallel RLC circuit, while additional LC tanks and parasitic elements account for the resonances introduced by the etched slots and ground modifications. This configuration effectively illustrates the multi-resonant behavior and aids in understanding how geometric features influence impedance matching and bandwidth enhancement. However, it is important to note that this lumped-element model approximates only the dominant resonant behavior near 9.1 GHz and does not fully capture the distributed electromagnetic effects responsible for the ultra-wideband response (9.1–100 GHz) observed in full-wave CST simulations and measurements.

Figure 9 shows that the surface current distribution of the proposed antenna was analyzed to understand the excitation of resonant modes at different frequencies. Figure 9(a) shows the current distribution at 20 GHz, while Figure 9(b) corresponds to 45 GHz. At 20 GHz, strong current density is concentrated around the feedline, central radiating patch, and circular slots near the lower edge of the antenna.

The distribution indicates that the currents are primarily localized along the edges of the etched slots, suggesting that these structural modifications play a significant role in exciting the lower-frequency resonances. The concentration of cur-

TABLE 2. The final equivalent circuit parameters for the proposed design.

Component	Description	Equivalent Values
Main Patch (Parallel RLC)	Radiation and storage	$R = 50\,\Omega$, $L = 1.02\,\text{nH}$, $C = 0.3\,\text{pF}$
Slot LC Tank 1	Resonance near 10 GHz	$L = 0.8\,\text{nH}$, $C = 0.25\,\text{pF}$
Slot LC Tank 2	Resonance near 14 GHz	$L = 0.5\,\text{nH}$, $C = 0.15\,\text{pF}$
Parasitic LC	Resonance near 19.5 GHz	$L = 1.5\,\text{nH}$, $C = 0.2\,\text{pF}$

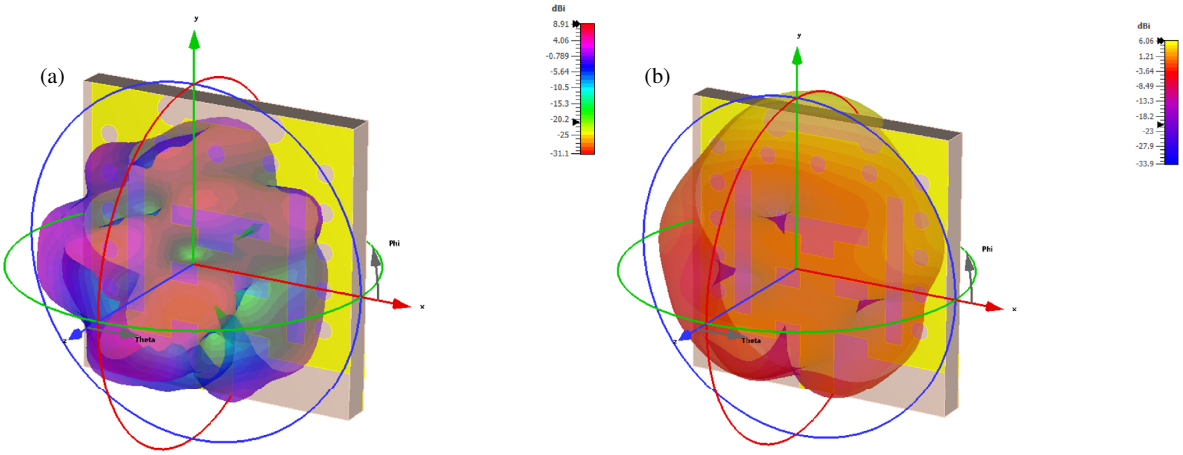

FIGURE 10. Radiation antenna 3-D lobe patterns at 20 and 45 GHz.

rents near the bottom cut-outs further confirms their influence on impedance matching at this band.

At 45 GHz, the current distribution becomes more complex, with high-density currents observed across the central slot region and along the vertical side slots. This indicates the excitation of higher-order modes, where multiple slots collectively contribute to resonance. The currents are spread more evenly across the patch, highlighting effective utilization of the radiating surface. This behavior ensures stable radiation patterns and improved bandwidth at millimeter-wave frequencies. Overall, the comparison shows that the etched slots and cut-outs are crucial for exciting resonances at both lower and higher bands, enabling the antenna to achieve ultra-wideband performance across 20 GHz and 45 GHz frequencies.

The 3D radiation characteristics of the proposed antenna were evaluated at two representative frequencies, 20 GHz and 45 GHz, to demonstrate its performance across the wide operating band. At 20 GHz (Figure 10(a)), the radiation lobe exhibits a multi-directional pattern with several smaller lobes surrounding the main beam. This indicates the excitation of multiple resonant modes at lower frequencies, where current crowding and slot interactions contribute to complex radiation behavior. The gain reaches a peak value of approximately 8.9 dBi, showing that the antenna delivers strong radiation with multiple active lobes, suitable for wide coverage applications. At 45 GHz (Figure 10(b)), the radiation pattern becomes more stable and directional than the 20 GHz case. The antenna radiates with fewer side lobes, and the energy is concentrated more effectively in the main lobe direction. The maximum gain achieved at this frequency is around 6 dBi, which, although slightly lower than at 20 GHz, demonstrates efficient performance at higher millimeter-wave frequencies.

Figure 11 shows that the input impedance of the antenna was analyzed in terms of both the real and imaginary components across the frequency range of 10–100 GHz. The plot shows that the real part of the impedance (black curve) fluctuates around the standard 50 Ω line, which indicates good impedance matching over a wide spectrum. At several resonant frequencies, the real impedance closely approaches 50 Ω, ensuring efficient power transfer between the feedline and radiating element. Peaks beyond 70 Ω and dips near 25 Ω are observed at certain frequencies, but these variations remain within an acceptable range for ultra-wideband operation.

The imaginary part of the impedance (red curve) oscillates between positive and negative values, reflecting the reactive nature of the antenna at different frequencies. These fluctuations correspond to the capacitive and inductive effects introduced by the etched slots and ground modifications. Importantly, at resonant frequencies where S_{11} dips are observed, the imaginary impedance approaches zero, confirming good resonance conditions.

Figure 12 illustrates the measured and simulated performances of the compact antenna with dimensions $15 \times 16 \times 1.5\,\text{mm}^3$, specifically focusing on its gain and efficiency characteristics across the frequency range of 9.1–100 GHz. Both curves exhibit strong agreement, confirming the validity of the design and the accuracy of the simulation model. The antenna demonstrates a consistent and stable radiation response, maintaining a peak gain of approximately 8.9 dBi and an efficiency nearing 89.8% over a wide frequency span. Minor variations observed between the simulated and measured plots are attributed to fabrication tolerances and connector losses at higher frequencies.

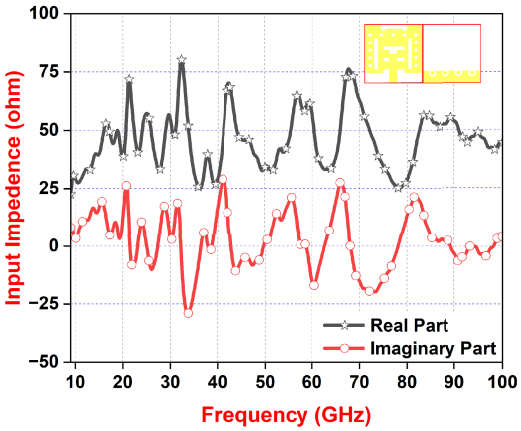

FIGURE 11. Input impedance of the proposed antenna.

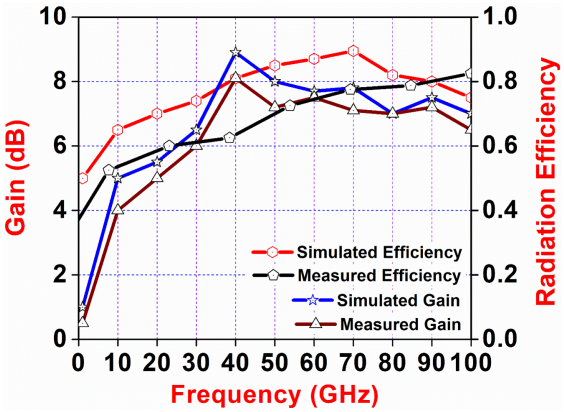

FIGURE 12. Gain and radiation curve.

TABLE 3. Comparison table of previously published articles.

Ref.	Frequency/Band	Size (mm^3)	Bandwidth (GHz)	Gain	Efficiency	Substrate
[2]	28 GHz	6.2 × 8.4 × 1.5	15.57 (19.9%)	5.06 dBi	≈ 80.2%	Rogers RT/Duroid 5880
[3]	38 & 54 GHz	26 × 30 × 1.5	1.94 & 2.05	6.9 dBi, 7.4 dBi	≈ 85.2%	Rogers RT/Duroid 5880
[5]	20/60/120 GHz	20 × 20 × 1.5	10–57 (102%)	6.06 dBi	≈ 81.2%	FR4 (1.5 mm)
[8]	10.15 GHz	20 × 20 × 1.6	380–400 MHz	4.46 dBi	≈ 86.2%	FR-4 (1.6 mm)
[14]	30/60/120 GHz	24 × 30 × 1.6	Survey (various)	7.1 dBi	≈ 82.2%	FR-4 (1.6 mm)
[16]	29.138 GHz	40 × 40 × 1.6	Broad/multi-band	8.1 dBi	Up to 94%	Rogers RO4450B
[17]	25–100 GHz	34 × 40 × 1.6	15.57(19.9%)	6.7 dBi	≈ 82.2%	FR-4 (1.6 mm)
[18]	28–65 GHz	20 × 20 × 1.6	(19–100) 146%	4.46 dBi	NR	FR-4 (1.6 mm)
[19]	17–100 GHz	32 × 40 × 1.5	15.57 GHz (19.9%)	6.06 dBi	≈ 80.2%	Rogers RT/Duroid 5880
Proposed	9.1100 GHz	15 ×16 ×1.5	(9.1–100) 166%	8.91 dBi	89.8%	FR-4

To validate the simulated design, the antenna was fabricated using standard photolithography on an FR4 substrate. The front and back views of the fabricated prototype are shown in Figure 13, where a measurement scale in centimeters has been included for dimensional verification. The visual comparison confirms that the fabricated antenna precisely matches the simulated design dimensions. The inclusion of the scale provides clear evidence of fabrication accuracy and supports the structural consistency between the simulated model and the practical prototype.

Table 3 presents a comparison of the proposed antenna with several reported millimeter-wave designs. The results show that the proposed design achieves a much wider impedance bandwidth (166%, 9.1–100 GHz) and a higher gain of 8.91 dBi with around 90% efficiency. These enhancements are mainly due to the optimized hybrid slot geometry and refined coupling between slot elements, which improve mode excitation and impedance matching. Unlike earlier designs limited to specific mmWave bands, the proposed antenna maintains continuous wideband operation across multiple frequency ranges using a cost-effective FR4 substrate, demonstrating strong practical and electromagnetic design advantages.

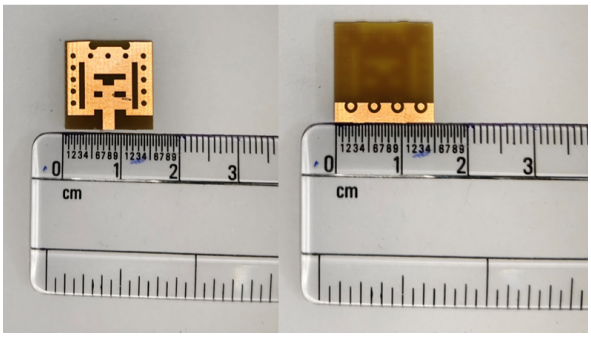

FIGURE 13. Front and rear views of the fabricated antenna prototype.

6. CONCLUSION

The proposed compact antenna, with dimensions of $15 \times 16 \times 1.5\,mm^3$, has been successfully designed, fabricated, and validated for millimeter-wave applications. It achieves an ultra-wide impedance bandwidth of 166% spanning 9.1–100 GHz, with measured and simulated results showing close agreement. The antenna offers a peak gain of 8.91 dBi, 89.8% efficiency, and stable radiation characteristics across the operating spectrum. Surface current and radiation analysis confirm the excitation of multiple resonant modes, providing multi-lobe radiation at 20 GHz and more directional behavior at 45 GHz. With its compact electrical size of $0.45\lambda \times 0.48\lambda \times 0.045\lambda$ at 9.1 GHz, the design ensures efficient integration into modern systems.

Overall, the antenna demonstrates a combination of wide bandwidth, high gain, and compactness, making it a promising candidate for X-, Ku-, K-, Ka-, V-, and W-band systems, including 5G, 6G, radar, satellite, and security imaging applications.

REFERENCES

[1] Mishra, B., R. K. Verma, R. K. Singh, *et al.*, "A review on microstrip patch antenna parameters of different geometry and bandwidth enhancement techniques," *International Journal of Microwave and Wireless Technologies*, Vol. 14, No. 5, 652–673, 2022.

[2] Przesmycki, R., M. Bugaj, and L. Nowosielski, "Broadband microstrip antenna for 5G wireless systems operating at 28 GHz," *Electronics*, Vol. 10, No. 1, 1, 2021.

[3] Imran, D., M. M. Farooqi, M. I. Khattak, Z. Ullah, M. I. Khan, M. A. Khattak, and H. Dar, "Millimeter wave microstrip patch antenna for 5G mobile communication," in *2018 International Conference on Engineering and Emerging Technologies (ICEET)*, 1–6, Lahore, Pakistan, Feb. 2018.

[4] Khidre, A., K.-F. Lee, A. Z. Elsherbeni, and F. Yang, "Wide band dual-beam U-slot microstrip antenna," *IEEE Transactions on Antennas and Propagation*, Vol. 61, No. 3, 1415–1418, 2013.

[5] Baudha, S., K. Kapoor, and M. V. Yadav, "U-shaped microstrip patch antenna with partial ground plane for mobile satellite services (MSS)," in *2019 URSI Asia-Pacific Radio Science Conference (AP-RASC)*, 1–5, New Delhi, India, Mar. 2019.

[6] Kurniawan, A. and S. Mukhlishin, "Wideband antenna design and fabrication for modern wireless communications systems," *Procedia Technology*, Vol. 11, 348–353, 2013.

[7] Ghosh, A., S. K. Ghosh, D. Ghosh, and S. Chattopadhyay, "Improved polarization purity for circular microstrip antenna with defected patch surface," *International Journal of Microwave and Wireless Technologies*, Vol. 8, No. 1, 89–94, 2016.

[8] Verma, S., L. Mahajan, R. Kumar, H. S. Saini, and N. Kumar, "A small microstrip patch antenna for future 5G applications," in *2016 5th International Conference on Reliability, Infocom Technologies and Optimization (Trends and Future Directions) (ICRITO)*, 460–463, Noida, India, Sep. 2016.

[9] Akyildiz, I. F., C. Han, and S. Nie, "Combating the distance problem in the millimeter wave and terahertz frequency bands," *IEEE Communications Magazine*, Vol. 56, No. 6, 102–108, Jun. 2018.

[10] Akyildiz, I. F., J. M. Jornet, and C. Han, "Terahertz band: Next frontier for wireless communications," *Physical Communication*, Vol. 12, 16–32, 2014.

[11] Han, C. and Y. Chen, "Propagation modeling for wireless communications in the terahertz band," *IEEE Communications Magazine*, Vol. 56, No. 6, 96–101, Jun. 2018.

[12] Rappaport, T. S., Y. Xing, O. Kanhere, S. Ju, A. Madanayake, S. Mandal, A. Alkhateeb, and G. C. Trichopoulos, "Wireless communications and applications above 100 GHz: Opportunities and challenges for 6G and beyond," *IEEE Access*, Vol. 7, 78 729–78 757, 2019.

[13] Jornet, J. M., E. W. Knightly, and D. M. Mittleman, "Wireless communications sensing and security above 100 GHz," *Nature Communications*, Vol. 14, No. 1, 841, 2023.

[14] Singh, C., C. Sharma, S. Tripathi, M. Sharma, and A. Agrawal, "A comprehensive survey on millimeter wave antennas at 30/60/120 GHz: Design, challenges and applications," *Wireless Personal Communications*, Vol. 133, No. 3, 1547–1584, 2023.

[15] Min, J.-S., S.-M. Moon, and H. L. Lee, "Low-profile radome-optimized high-gain series-fed array antenna for W-band radar applications," *Alexandria Engineering Journal*, Vol. 125, 388–398, 2025.

[16] Al-Hiti, A. S., A. K. Ahmed, S. H. Mhmood, and B. I. Hamdallah, "Broadband and multiband millimeter wave microstrip patch antenna for 5G and 6G applications," *Journal of Umm Al-Qura University for Engineering and Architecture*, Vol. 16, No. 3, 720–731, 2025.

[17] Perez-Palomino, G., M. Barba, J. A. Encinar, R. Cahill, R. Dickie, P. Baine, and M. Bain, "Design and demonstration of an electronically scanned reflectarray antenna at 100 GHz using multiresonant cells based on liquid crystals," *IEEE Transactions on Antennas and Propagation*, Vol. 63, No. 8, 3722–3727, 2015.

[18] Kumar, P., T. Ali, O. P. Kumar, S. Vincent, P. Kumar, Y. Nanjappa, and S. Pathan, "An ultra-compact 28 GHz arc-shaped millimeter-wave antenna for 5G application," *Micromachines*, Vol. 14, No. 1, 5, 2023.

[19] Muttair, K. S., O. A. Shareef, H. B. Taher, and F. Arith, "A new geometry of multi-band MIMO antenna for 5G and 6G systems," *Journal of Techniques*, Vol. 6, No. 4, 48–56, 2024.

[20] Khidre, A., K. F. Lee, F. Yang, and A. Elsherbeni, "Wideband circularly polarized E-shaped patch antenna for wireless applications [wireless corner]," *IEEE Antennas and Propagation Magazine*, Vol. 52, No. 5, 219–229, Oct. 2010.

[21] Baudha, S., K. Kapoor, and M. V. Yadav, "U-shaped microstrip patch antenna with partial ground plane for mobile satellite services (MSS)," in *2019 URSI Asia-Pacific Radio Science Conference (AP-RASC)*, 1–5, New Delhi, India, 2019.

[22] Marotkar, D. S. and P. Zade, "Bandwidth enhancement of microstrip patch antenna using defected ground structure," in *2016 International Conference on Electrical, Electronics, and Optimization Techniques (ICEEOT)*, 1712–1716, Chennai, India, 2016.